Controls on the formation of Fe(II,III) (hydr)oxides by Fe(0) electrolysis

C.M. van Genuchten [a, b, *], T. Behrends [a], P. Kraal [a], S.L.S. Stipp [b], K. Dideriksen [b]

[a] Department of Earth Sciences − Geochemistry, Faculty of Geosciences, Utrecht University, Utrecht, 3508TA, The Netherlands
[b] Nano-Science Center, Department of Chemistry, University of Copenhagen, Copenhagen, Denmark

ARTICLE INFO

ABSTRACT

This study identifies the electrochemical and solution chemical controls on the production of Fe(II,III) (hydr)oxides formed by the electrolysis of Fe(0) metal, also knows as Fe(0) electrocoagulation. EXAFS spectroscopy and X-ray diffraction were used to characterize the solids produced as a function of: i) applied current, which corresponded to iron(II) production rates of $30-300\,\mu M\,min^{-1}$, ii) pH and iii) background electrolyte. Two systems were investigated where: i) the dissolved oxygen (O_2) concentration was maintained at 0.1, 0.3 and $3.0\,mg\,L^{-1}$ and ii) the O_2 drifted in response to varied Fe(II) addition rates. A narrow range of O_2 separated the domains for Fe(II,III) and Fe(III) (hydr)oxide formation. At $O_2 \geq 0.3\,mg\,L^{-1}$, Fe(III) solids dominated, while Fe(II,III) (hydr)oxides were the principal phases at $O_2 = 0.1\,mg\,L^{-1}$. The highest fraction of Fe(II,III) (hydr)oxides formed in the O_2 drift experiments at the highest Fe(II) production rate, i.e. $300\,\mu M\,min^{-1}$. The background electrolyte determined the type of Fe(II,III) (hydr)oxide that formed: NaCl solutions favored magnetite and $NaHCO_3$ solutions favored carbonate green rust. Our results are consistent with an Fe(II,III) (hydr)oxide formation pathway where Fe(II) addition after O_2 depletion leads to rapid (<10 min) transformation of precursory Fe(III) precipitates.

© 2018 Elsevier Ltd. All rights reserved.

1. Introduction

Mixed valent Fe(II,III) (hydr)oxides exhibit remarkable properties relative to their Fe(III) counterparts because of their unique structures and the presence of Fe(II). These properties make Fe(II,III) (hydr)oxides especially suitable for implementation in remediation strategies. For example, the layered double hydroxide, green rust (GR, $[Fe^{II}_{(1-x)}Fe^{III}(OH)_2]^{x+}\cdot[(x/n)A^{n-}\cdot(mx/n)H_2O]^{x-}$ where A^{n-} are anions, including Cl^- and CO_3^{2-}), is a powerful reductant that has been studied extensively for its role in the reductive transformation of inorganic and organic contaminants [1–4]. In addition, GR is an effective scavenger of contaminants such as arsenic (As) because of its abundant reactive sorption sites on particle edges [5,6]. The Fe(II,III) oxide, magnetite ($Fe^{II}Fe^{III}_2O_4$), is a spinel type mineral that in its ideal form contains 33% tetrahedrally coordinated Fe. By substituting for tetrahedrally coordinated Fe, pyramidal or tetrahedral oxyanions (e.g. As(III), As(V)) have been proposed to incorporate into the magnetite structure or to sorb in highly stable multidentate configurations on magnetite surfaces [7–9]. Magnetite formation is also strategic for contaminant removal since contaminant laden magnetite suspensions can be separated from solution easily and at low cost using low strength magnetic fields [10]. Because of the exceptional reactivity of Fe(II,III) (hydr)oxides, the formation pathways of these minerals are of considerable interest [11,12].

One unconventional method of producing Fe(II,III) (hydr)oxides uses electrolysis of sacrificial Fe(0) electrodes [15–17]. This method, also known as Fe(0) electrocoagulation (EC), has been proposed as a decentralized water treatment method [18], in part because of its low infrastructure requirements [19] and its effective removal of a variety of contaminants, including arsenic, chromium, uranium and pathogens [20–22]. In Fe(0) EC, an electric current is applied to Fe(0) electrodes in contact with an electrolyte solution to produce Fe(II) ions [23]. The soluble Fe(II) ions are oxidized by dissolved oxygen (O_2) to produce reactive Fe precipitates, the structures of which depend on the EC operating parameters and solution composition. By selectively producing Fe(II,III) (hydr)oxides, Fe(0) EC systems could exploit the unique properties of these minerals to improve treatment performance. Knowledge about the formation conditions of Fe(II,III) (hydr)oxides by Fe(0) EC would also be important to constrain the chemical conditions required for formation in natural systems.

* Corresponding author. Department of Earth Sciences − Geochemistry, Faculty of Geosciences, Utrecht University, Utrecht 3508TA, The Netherlands.
E-mail address: c.m.vangenuchten@uu.nl (C.M. van Genuchten).

The production of Fe(II,III) (hydr)oxides has been reported in some Fe(0) EC studies [24,25]. However, systematic investigations of the EC system conditions required for the formation of Fe(II,III) (hydr)oxides are largely absent in the literature [26]. The primary product of Fe(0) EC is Fe(II), which can be further oxidized by O_2. Incomplete oxidation of Fe(II) is a prerequisite for the formation of mixed redox state Fe (hydr)oxides, thus it is hypothesized that the initial O_2 concentration and the balance between O_2 consumption by Fe(II) oxidation and dissolution of atmospheric O_2 during Fe(0) electrolysis are the primary factors controlling whether Fe(II,III) (hydr)oxides form. One of the key technical aspects of Fe(0) EC systems is that the applied current is directly related to the Fe(II) production rate [27]. Therefore, the interplay between Fe(II) production rate and the O_2 concentration is examined systematically in this study, in view of the characteristics of the formed EC products.

The pH and composition of the electrolyte solution are expected to impact Fe(II,III) (hydr)oxide formation in addition to the Fe(II) production rate and O_2. Fig. 1 illustrates that at typical dissolved Fe concentrations, the formation of Fe(II,III) (hydr)oxides is thermodynamically feasible at pH above $\approx 6-7$ [28–30]. The anion composition of the solution is also an important variable, particularly for GR formation, because GR stability depends on its interlayer anion, with stability increasing in the order: chloride < sulfate < carbonate [2,31]. Because the electrolyte solution can modify Fe(II,III) (hydr)oxide structure and composition, it is essential to investigate the formation of Fe(II,III) phases across a broad range of pH and in the presence of different anions that are ubiquitous in the environment.

Our objective was to determine the electrochemical and solution chemical controls on the formation of Fe(II,III) (hydr)oxides by Fe(0) EC. To this end, suspensions of 3 mM total Fe were generated by Fe(0) electrolysis, using a range of applied currents that correspond to iron(II) production rates from 30 to 300 $\mu M\,min^{-1}$. Two experimental systems were investigated: i) a controlled O_2 system, where O_2 was held constant at levels ranging from 0.1 to 3.0 $mg\,L^{-1}$ and ii) a system where O_2 was allowed to drift in response to a range of Fe(II) production rates. To encompass a variety of solution

compositions, pH was varied from 7 to 10 and different background electrolyte compositions (10 mM NaCl or 10 mM $NaHCO_3$) were examined in the controlled O_2 and O_2 drift experiments. The solid phases formed in the experiments were determined by X-ray diffraction (XRD) and Fe K-edge extended X-ray absorption fine structure (EXAFS) spectroscopy. The Fe(II,III) (hydr)oxide formation conditions identified in this work can be used to inform the design of Fe(II,III) (hydr)oxide-based remediation strategies and advance the understanding of the conditions and pathways for Fe(II,III) phase formation in natural systems, particularly where fluxes of Fe(II) and O_2 meet at redox boundaries.

2. Materials and methods

2.1. Materials

Stock solutions of 0.5 M NaCl and 0.3 M $NaHCO_3$ were prepared by adding the corresponding salts to 1.0 L of 18 $M\Omega$ cm Milli-Q ultrapure deionized (DI) water. To adjust the pH of the stock solutions to 7, 8.5 or 10, NaOH and either HCl (for the NaCl solution) or $CO_{2(g)}$ (for the $NaHCO_3$ solution) were used. After preparation, the stock solutions were stored in air tight containers at room temperature. Electrolyte solutions for the Fe(0) EC experiments were prepared by mixing stock solutions and DI water to yield 10 mM concentrations of chloride or dissolved inorganic carbon (herein referred to as carbonate for brevity). We learned in our previous Fe(0) EC study [32], that a small amount of chloride is required to produce Fe(II) rather than O_2 during Fe(0) electrolysis in carbonate solutions (molar ratio of carbonate to chloride must be < 100). Therefore, 0.3 mM NaCl was added to the carbonate solutions, which resulted in <5% difference in the initial ionic strength for the two electrolyte solutions.

Reference Fe-bearing material was synthesized following procedures reported previously [4,33–35] and included magnetite, green rust, lepidocrocite, ferrihydrite and Si-rich hydrous ferric oxide (Si-HFO). The synthesis methods for the reference material are described in the Supplementary Data.
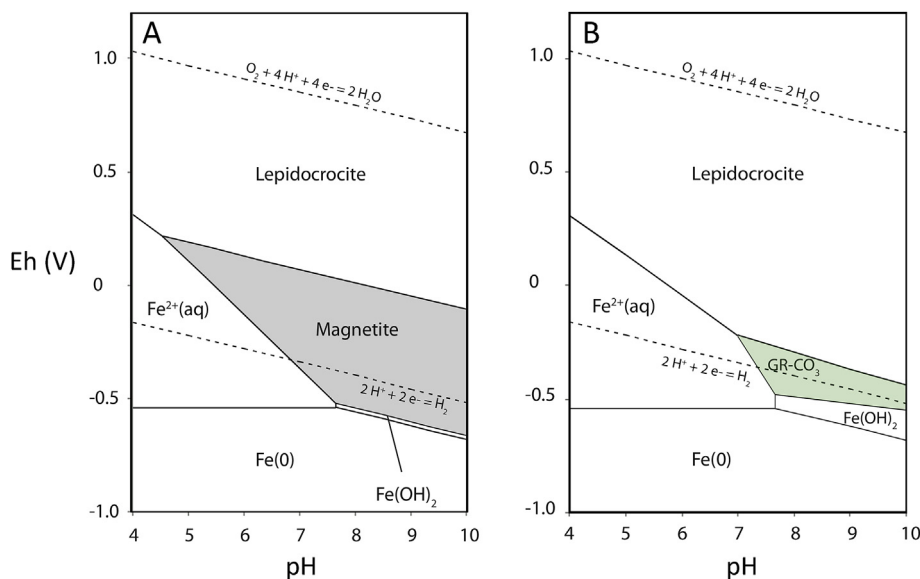
Fig. 1. Pourbaix diagrams for 3 mM Fe in the presence of 10 mM NaCl (A) or 10 mM $NaHCO_3$ (B). Thermodynamic data used in the calculations were obtained from Robie and Hemmingway [61], Feitknecht and Schindler [73] and Drissi et al. [56]. The shaded green region represents the stability field for GR, whereas the shaded grey region represents the stability field of magnetite. Magnetite was excluded from the calculations for Panel B. Lepidocrocite is metastable, but is the primary crystalline Fe(III) precipitate formed during Fe(II) oxidation [48] and therefore other Fe(III) precipitates have been excluded. (For interpretation of the references to color in this figure legend, the reader is referred to the Web version of this article.)

2.2. Electrocoagulation experiments

2.2.1. Fe(0) EC reactor setup

Electrocoagulation experiments were performed in 200 mL electrolyte solutions in Teflon reactor vessels using an overhead glass stirrer for mixing. Acid washed Fe(0) electrodes with 10 cm^2 submerged surface area served as the anode and cathode. The electrodes were spaced ~1 cm apart. Controlled O$_2$ experiments were performed in sealed Teflon reactors with ports drilled in the Teflon lids for pH and O$_2$ measurements, sampling, gas inlet and outlet and overhead mixing (Fig. S1 in the Supplementary Data). For this set of the experiments, the initial O$_2$ was set and maintained at 3.0, 0.3 and 0.1 mg L^{-1} throughout Fe(0) electrolysis by bubbling mixtures of air and N$_{2(g)}$ using gas flow regulators. The O$_2$ was logged with a Hach IntelliCAL optical O$_2$ probe throughout electrolysis and the mixtures of N$_{2(g)}$ and air were adjusted carefully during the experiment to ensure the O$_2$ levels were constant (the O$_2$ variation for a representative controlled O$_2$ experiment is presented in the Supplementary Data, Fig. S2).

The O$_2$ drift experiments were also performed in Teflon reactors but the lid was not used and the solutions were exposed to the atmosphere throughout the 10—100 min reactions. The effects of evaporation on solution concentrations were assumed to be negligible in the timescales of these experiments. In the O$_2$ drift experiments, the O$_2$ concentration was set initially to 3.0 mg L^{-1} by bubbling with N$_{2(g)}$ and the O$_2$ was left to drift during Fe(0) electrolysis. We chose O$_2 = 3.0$ mg L^{-1} because low O$_2$ levels are typical in As contaminated groundwater in South Asia [36], a major target area for As remediation using Fe(II,III) (hydr)oxides generated by Fe(0) EC [37]. We note that CO$_{2(g)}$ from air was not excluded in the controlled O$_2$ and O$_2$ drift experiments, which could add a minor fraction of dissolved inorganic carbon to the chloride solution experiments. Likewise, CO$_{2(g)}$ would exsolve from the lower pH carbonate solutions. However, the influence of CO$_{2(g)}$ dissolution and exsolution on Fe(II,III) (hydr)oxide formation is expected to be minimal because of the low carbonate concentrations in equilibrium with air and because the EC experiments are so short (10 min for high IPR experiments) that only minor CO$_{2(g)}$ equilibration is expected. A summary of the experimental conditions for all EC samples is given in Table 1.

In addition to Fe(0) EC experiments, a series of tests was performed to quantify the impact of solution mixing rate and exposed solution area to volume ratio on the rate of O$_2$ increase. In these experiments, O$_2$ was set to <0.5 mg L^{-1} by bubbling N$_{2(g)}$ in reactors of different sizes. The O$_2$ was then left to equilibrate with the atmosphere in the absence of Fe(0) electrodes under a range of mixing rates.

2.2.2. Fe(0) EC cell operation

Precipitates were generated by applying a galvanostatic current to the EC cell to generate a total charge dosage of 600 C L^{-1}. This charge dosage corresponds to 3 mM total Fe by Faraday's law, [Fe] = $I·t_e/(V·n·F)$, where I represents the current (C s^{-1}) applied for electrolysis time t_e (s), V represents the solution volume (L), n the number of electrons transferred (2 for Fe(II) formation) and F represents Faraday's constant (96,485 C mol^{-1}). Measurements of total Fe generated at the end of Fe(0) electrolysis revealed a Faradaic efficiency typically > 0.95, confirming the formation of Fe(II) during electrolysis, which is consistent with previous Fe(0) EC studies [23,27]. The range of investigated currents (0.02–0.2 C s^{-1}) correspond to iron(II) production rates (Fe(II) production rates) of 30–300 μM min^{-1} and total electrolysis times of 10–100 min. Solution pH was manually adjusted using dilute HCl during electrolysis to balance the increase in pH resulting from H$^+$ reduction at the cathode. The typical variation in pH of the bulk solution throughout

Table 1
Summary of Experimental Conditions.

	Initial Dissolved Oxygen (mg L^{-1})	pH	Background Electrolyte[a]	Fe(II) Production Rate (μM Fe(II) min^{-1})
Controlled Dissolved Oxygen System	3.0	7	NaCl	300
	0.3	7	NaCl	300
	0.1	7	NaCl	300
	3.0	8.5	NaCl	300
	0.3	8.5	NaCl	300
	0.1	8.5	NaCl	300
	3.0	10	NaCl	300
	0.3	10	NaCl	300
	0.1	10	NaCl	300
	3.0	7	NaHCO$_3$	300
	0.3	7	NaHCO$_3$	300
	0.1	7	NaHCO$_3$	300
	3.0	8.5	NaHCO$_3$	300
	0.3	8.5	NaHCO$_3$	300
	0.1	8.5	NaHCO$_3$	300
	3.0	10	NaHCO$_3$	300
	0.3	10	NaHCO$_3$	300
	0.1	10	NaHCO$_3$	300
Dissolved Oxygen Drift System	3.0	7	NaCl	30
	3.0	7	NaCl	100
	3.0	7	NaCl	300
	3.0	10	NaCl	30
	3.0	10	NaCl	100
	3.0	10	NaCl	300
	3.0	7	NaHCO$_3$	30
	3.0	7	NaHCO$_3$	100
	3.0	7	NaHCO$_3$	300
	3.0	10	NaHCO$_3$	30
	3.0	10	NaHCO$_3$	100
	3.0	10	NaHCO$_3$	300

^a The concentrations of the NaCl and NaHCO$_3$ solutions were 10 mM.

the experiments was less than ±0.3 but pH gradients near the electrodes during Fe(0) electrolysis can occur that are not accounted for by bulk pH measurements. Whereas CO$_{2(g)}$ was used to set the pH of the carbonate stock solutions, HCl was used to counter any pH increase during electrolysis because of CO$_2$ outgassing during carbonate solution experiments, which would decrease the supersaturation of carbonate-bearing phases.

Aliquots of the suspension were sampled at the end of electrolysis, filtered immediately through 0.22 μm filters and acidified with HNO$_3$ for subsequent analysis of aqueous Fe by atomic absorption spectroscopy (AAS, Perkin Elmer AAnalyst 800). Unfiltered aliquots were also taken at the end of electrolysis and acidified for AAS measurements to determine the total Fe that had been dosed by Fe(0) EC. After electrolysis, the reactor was sealed with an air tight lid and the suspension was transported immediately to an anaerobic chamber to collect and prepare the solids for characterization.

2.3. X-ray diffraction

Samples for powder X-ray diffraction (XRD) were obtained by filtering the precipitate suspension within an anaerobic chamber using 0.22 μm filters. The filtered solids were dried in the anaerobic chamber and ground into a powder using an agate mortar and pestle. Powder diffraction patterns were collected during contact with the atmosphere, using a Bruker D8 Advance diffractometer with Cu K-alpha radiation, a rotating sample stage and an energy dispersive detector to suppress fluorescence. Data were collected for 5—75° 2θ with 0.02° step size and total data collection time of ~4 h per sample. Because of the potential for oxidation of the Fe(II,III) (hydr)oxides during XRD data collection in air, the impact

of adding a small volume (<1 mL) of glycerol was tested on samples containing magnetite and GR-CO$_3$. The XRD patterns of magnetite with and without glycerol were indistinguishable but glycerol was required to prevent GR-CO$_3$ transformation during analysis. Therefore, following previous procedures [38], glycerol was added to preserve samples during XRD (and EXAFS) analysis. The X-ray diffractograms are reported with different intensity scaling to simplify comparison among solids with different crystallinity.

2.4. Extended X-ray absorption fine structure spectroscopy

2.4.1. Sample preparation and data collection

Solids for EXAFS analysis (roughly 20 mg) were collected on 0.22 μm filters within an anaerobic chamber, loaded as wet pastes into custom sample holders and encapsulated in Kapton tape. To optimize data collection in transmission mode, an appropriate volume of suspension was filtered to ensure that the total absorption from the entire sample was less than 2.5 absorption lengths, while the absorption of Fe was 1.0 absorption length [39]. Glycerol was added to all samples prior to loading in sample holders to minimize oxidation by air diffused through the Kapton tape during measurements. After loading all samples, each sample holder was sealed in an anaerobic container and transferred to a 1 °C storage unit until transport to the beam line in containers cooled with ice packs.

Fe K-edge EXAFS data were collected at the DUBBLE beam line (BM-26a) of the European Synchrotron Radiation Facility (ESRF). The design of the beamline is described by Borsboom et al. [40] and Nikitenko et al. [41]. Spectra were recorded at room temperature in transmission mode out to $k = 13$ Å^{-1}. The vertical dimension of the X-ray beam during the measurement was ~1 mm and the horizontal dimension was 3 mm. Harmonic rejection mirrors were used to prevent second order harmonics. The XANES region was measured with 0.35 eV steps, while a step size of 0.05 Å^{-1} was used for the EXAFS region. Two to four scans were collected for each sample. Spectra were also collected for sulfate green rust, magnetite, lepidocrocite, 2-line ferrihydrite and Si-HFO references. A Fe(0) foil was used to calibrate the beam at 7112 eV, at the maximum slope of the main absorption edge. During data collection, particular consideration was given to comparing changes in line shape and peak position indicative of sample oxidation. Our method to avoid oxidation artifacts during data collection was confirmed by the identical XANES and EXAFS spectra from a green rust reference sample, measured at the start and end of the experiment (Fig. S3 in the Supplementary Data). Spectra were aligned, averaged and background subtracted using SixPack software [42] following standard methods described previously [43].

2.4.2. Iterative transformation factor analysis

Principal component analysis (PCA) and iterative transformation factor analysis (ITFA) of the Fe K-edge EXAFS spectra ($k = 2$–12 Å^{-1}) were performed using the ITFA software package [44] following previous procedures [45,46]. The number of unique (principal) components that reproduced the major variance in the experimental data set (number of spectra, $N = 30$) was determined using the minimum of the indicator function (IND) [44]. The entire experimental data set was reconstructed using the number of principal components by varying the relative concentration of each component. For this step, ITFA requires that the relative concentration of at least one of the components be constrained to 1.0 in one sample. Thus, the relative contribution of two of the components was constrained to 1.0 for spectra obtained in O$_2$ drift experiments with the highest Fe(II) production rate at pH 7 in the chloride and carbonate solutions. These spectra showed the highest loading with the respective component after the Varimax rotation

and the XRD data contained only Bragg peaks of magnetite or GR-CO$_3$, implying that no other crystalline phases were present in significant amounts. Components determined to have relative concentrations <0.1 have not been reported. Relative concentrations derived by ITFA were normalized to 1.0. The ITFA analysis permits extracting endmember spectra from a data set containing mixtures of these endmembers. The endmember spectra derived in this approach were compared with the EXAFS spectra of Fe-bearing reference minerals that were analyzed by standard shell-by-shell fitting (Supplementary Data, Fig. S4, Table S1).

3. Results

3.1. Diversity of Fe phases formed by continuous Fe(II) addition

Peak intensities in the X-ray diffractograms varied systematically with changes in pH, O$_2$ concentration and composition of the solution (Figs. 2–5). Based on characteristic XRD peak position and intensity, four distinct mineral phases could be identified: i) carbonate green rust (GR-CO$_3$), ii) magnetite, iii) lepidocrocite and iv) a poorly ordered phase giving rise to the broad diffraction peaks consistent with ferrihydrite. For the principal component analysis of the EXAFS spectra for all 30 samples, including those from controlled O$_2$ and O$_2$ drift systems and chloride and carbonate solutions, the indicator function (IND) yielded a minimum with four components (Supplementary Data, Fig. S5). These results indicate that the solids obtained under a broad range of conditions are composed of four different Fe phases, which agrees with the XRD analysis. Therefore, the EXAFS spectra for all samples were reconstructed using linear combinations of four components. The four corresponding endmember spectra extracted by iterative target transformation (ITT) analysis are compared to EXAFS spectra for Fe-bearing reference minerals in Fig. 6.

Component 1 reproduced all fingerprints from the EXAFS spectrum of GR (Fig. 6A), including the subtle beat features near 7.6, 8.6 and 9.8 Å^{-1}. The lower intensity of the oscillations at k > 8 Å^{-1} in the target transformation of Component 1 relative to those of the GR reference spectrum produced a lower amplitude of the second shell peak (R + ΔR ≈ 2.8 Å), which arises from edge sharing Fe-Fe octahedra [47]. These differences suggest that the reference GR mineral is slightly more ordered along the sheets of edge sharing octahedra than the GR represented by Component 1. Component 2 was an excellent match to the EXAFS spectrum for magnetite (Fig. 6B), with only slight differences in the amplitudes of oscillations at $k > 9.4$ Å^{-1}. The corresponding Fourier transforms (Fig. 6F) suggest that these small differences arise from a lower contribution of corner sharing Fe-Fe atoms (R + ΔR ≈ 3.0 Å) and fewer next nearest neighbor Fe atoms (R + ΔR ≈ 4.7 Å), which implies that Component 2 represents a magnetite with slightly less structural order than the magnetite reference mineral.

Component 3 (Fig. 6C) closely matched the lepidocrocite reference EXAFS spectrum. The line shape and amplitude of the EXAFS spectra and the peak positions and amplitudes in the Fourier transforms are almost identical for Component 3 and the reference lepidocrocite. Component 4 was similar to the EXAFS spectrum of 2-line ferrihydrite but was slightly out of phase with the major oscillations at 6.2 and 8.3 Å^{-1} and the more broad oscillations at k > 10 Å^{-1}. These deviations are manifest in a lower second shell amplitude of the Fourier transformed EXAFS spectrum relative to that of 2-line ferrihydrite (Fig. 6H). Comparing Component 4 to the spectrum of Si-rich hydrous ferric oxide (Si-HFO), a precipitate that consists dominantly of edge sharing Fe octahedra [34,48,49], reveals a better match in the phase of the major peaks at 6.2 and 8.3 Å^{-1} and the oscillations at k > 10 Å^{-1} but a poor reproduction of the small features at 5.5 and 7.5 Å^{-1}. The corresponding Fourier
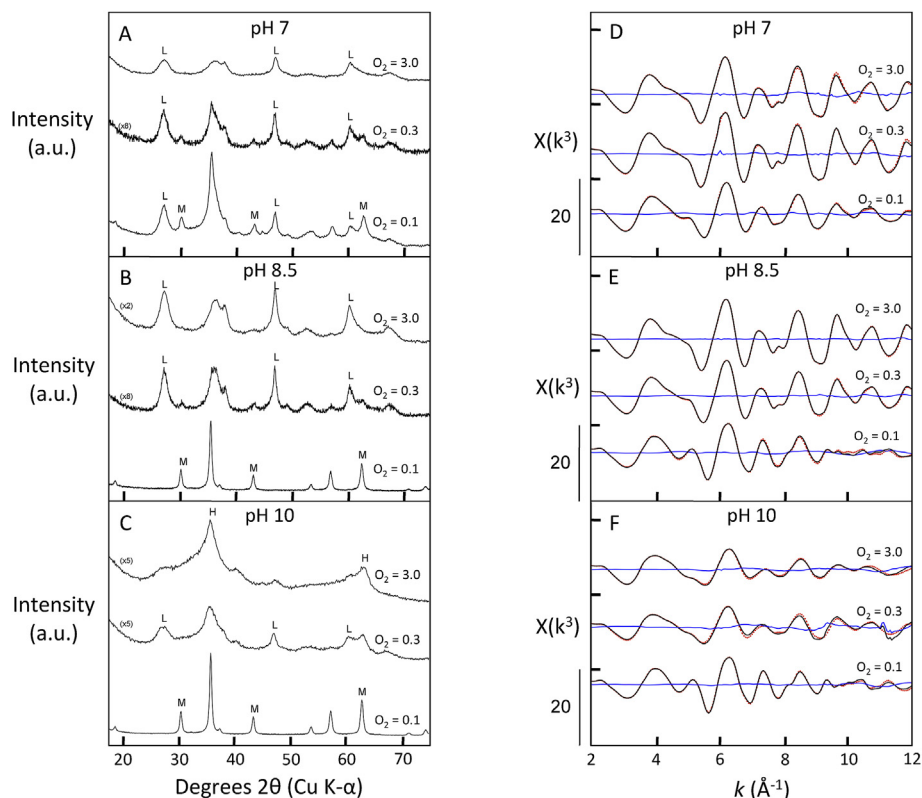
Fig. 2. XRD patterns (A–C) and Fe K-edge EXAFS spectra (D–F) of precipitates generated in chloride solution (pH 7, 8.5 and 10) at controlled O_2 concentrations of 3.0, 0.3 and 0.1 mg L^{-1}. Major peaks in the XRD data are indicated for magnetite (M), lepidocrocite (L) and hydrous ferric oxide (H). For the Fe K-edge EXAFS spectra, the black lines represent the data, the red dots represent the ITFA derived fits and the blue lines show the residual. (For interpretation of the references to color in this figure legend, the reader is referred to the Web version of this article.)

transform (Fig. 6H) shows that the shoulder at larger R in the second shell amplitude of Component 4, which arises from corner sharing Fe-Fe bonds, is greater than that of Si-HFO. Therefore, Component 4 represents a poorly crystalline Fe(III) precipitate with less Fe-Fe polyhedral connectivity than 2-line ferrihydrite, but more corner sharing Fe-Fe linkages than Si-HFO.

Based on this analysis of the target transformations, the components derived by ITT analysis are referred to as GR (Component 1), magnetite (Component 2), lepidocrocite (Component 3) and hydrous ferric oxide (HFO, Component 4).

3.2. Chloride solution: controlled O_2 system

3.2.1. X-ray diffraction

The XRD patterns for the precipitates generated in the controlled O_2 chloride solution (Fig. 2A–C) depend strongly on the O_2 concentration and solution pH. At the highest O_2 concentration of 3.0 mg L^{-1}, no peaks from Fe(II,III) (hydr)oxides, such as magnetite or chloride green rust (GR-Cl), were present, regardless of pH. Trends in the intensity of XRD peaks indicate a transition from lepidocrocite at pH 7 and 8.5 to poorly crystalline HFO at pH 10. A decrease in the O_2 from 3.0 to 0.1 mg L^{-1} produced a systematic increase in the intensity of the most pronounced Bragg peak of magnetite near 36° 2θ for all samples as well as growth of the (220), (400) and (440) magnetite peaks at ~30°, ~43° and ~63° 2θ. At these positions, lepidocrocite displays only minor peaks. The relative contribution of magnetite peaks to each XRD pattern depended on pH. At pH 7, peaks for both lepidocrocite and magnetite appeared in the $O_2 = 0.1$ mg L^{-1} sample, whereas the pH 8.5 and 10 samples were dominated by peaks characteristic of

magnetite. Although increasing pH from 8.5 to 10 substantially decreased the crystallinity of the Fe(III) precipitates generated at $O_2 = 3.0$ mg L^{-1}, the X-ray diffractograms for the pH 8.5 and 10 samples at $O_2 = 0.1$ mg L^{-1} were almost identical, suggesting that pH did not impact the long range order of the EC generated magnetite.

3.2.2. Iterative transformation factor analysis

Trends in changing mineralogy derived from the X-ray diffractograms for controlled systems samples in the chloride solution are further substantiated by the analysis of EXAFS spectra. At $O_2 = 3.0$ mg L^{-1}, the solids consisted exclusively of mixtures of lepidocrocite and HFO (Fig. 7), with pH 7 and 8.5 samples dominated by lepidocrocite (>0.8) and the pH 10 sample consisting primarily of HFO (0.85). Decreasing the O_2 by a factor of 10, from 3.0 to 0.3 mg L^{-1}, increased the abundance of lepidocrocite in samples generated at pH 7 (0.83–1.0) and pH 10 (0.15–0.4). At the same O_2 level and intermediate pH of 8.5, magnetite was detected but was still only a minor fraction (<0.25) of the solid phase. In contrast, a three fold decrease in O_2 from 0.3 to 0.1 mg L^{-1} led to a strong increase in the abundance of magnetite at all pH. The solids produced at pH 8.5 and 10 at $O_2 = 0.1$ mg L^{-1} consisted primarily of magnetite (>0.7), whereas the pH 7 sample contained similar fractions of magnetite (0.28), lepidocrocite (0.4) and HFO (0.33).

3.3. Chloride solution: O_2 drift system

#### 3.3.1. Time evolution of dissolved oxygen

In the O_2 drift system, the O_2 (Fig. 3) was largely controlled by the Fe(II) production rate. At the lowest Fe(II) production rate of

pH 7   ## pH 10
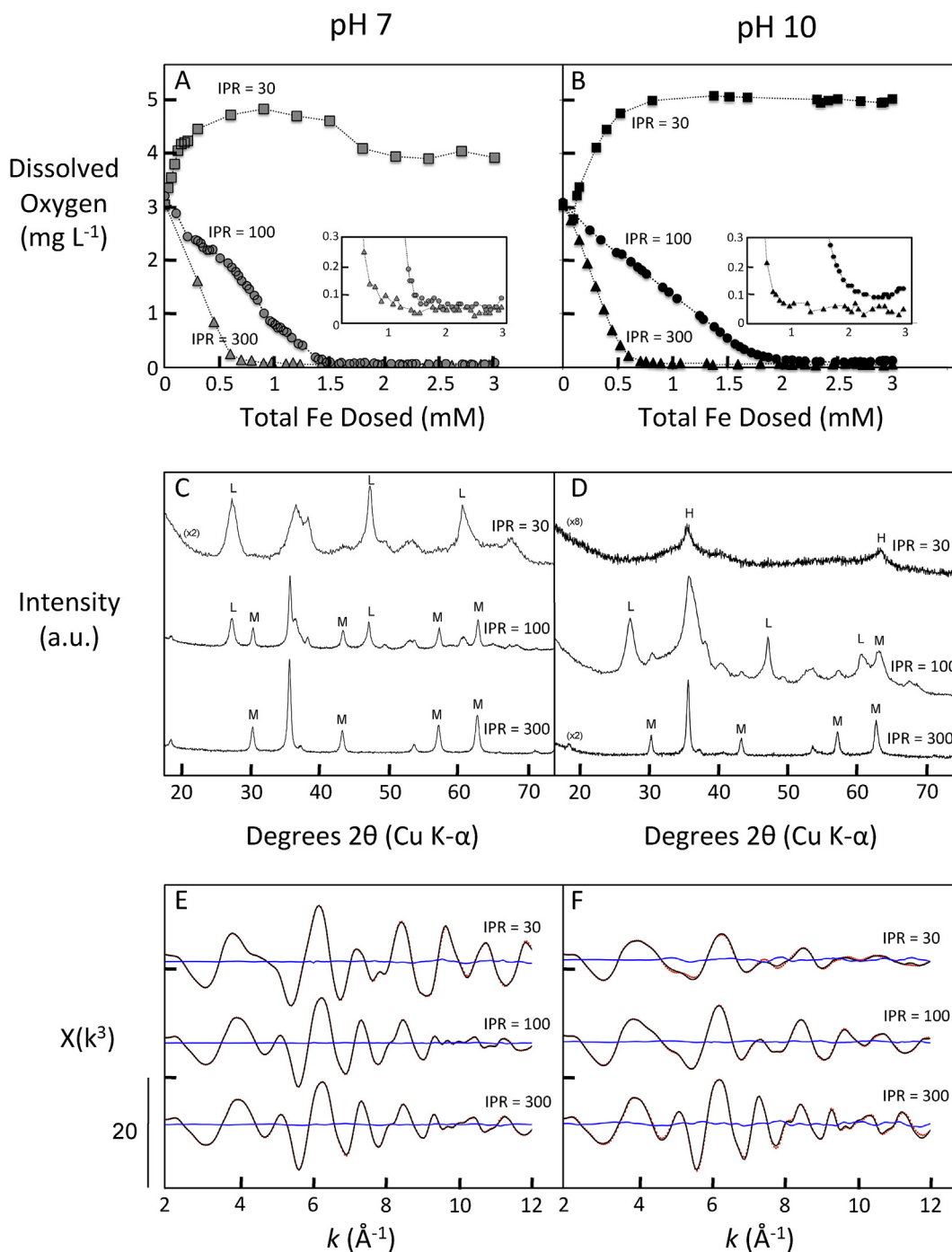
Fig. 3. Results for the O$_2$ drift system in the chloride solution: dissolved oxygen measurements (A, B), XRD patterns (C, D) and Fe K-edge EXAFS spectra (E, F). The left and right columns represent experiments at pH 7 and pH 10. The total Fe dosed in A and B corresponds to a Faradaic efficiency of 1.0. Major peaks in the XRD data are indicated for magnetite (M), lepidocrocite (L) and hydrous ferric oxide (H). For the Fe K-edge EXAFS spectra, the black lines represent the data, the red dots represent the ITFA derived fits and the blue lines show the residual. The Fe(II) production rate is abbreviated by IPR. (For interpretation of the references to color in this figure legend, the reader is referred to the Web version of this article.)

30 μM min^{-1}, the O$_2$ concentration increased from 3.0 mg L^{-1} to peak at O$_2$ ~5 mg L^{-1} at both pH 7 and 10. The time evolution of O$_2$ in these experiments indicates that the rate of O$_2$ consumption by Fe(II) was lower than the influx of O$_2$ from air during the initial stage of Fe(0) electrolysis, after which a steady state developed. However, for the pH 7 experiment, the O$_2$ subsequently decreased to ~4 mg L^{-1} after reaching a maximum, which implies that Fe(II) oxidation rates increased during the course of this experiment,

most likely resulting from heterogeneous Fe(II) oxidation induced by the formation of Fe (hydr)oxides. At the end of both the pH 7 and pH 10 experiments at Fe(II) production rate = 30 μM min^{-1}, aqueous Fe was not detected (Table S2), which is consistent with the rapid oxidation rates of Fe(II) at O$_2$ > 3.0 mg L^{-1}. When the Fe(II) production rate was set at 100 μM min^{-1}, the O$_2$ in the pH 7 experiment depleted rapidly, leading to O$_2$ < 0.1 mg L^{-1} for the remaining ~40% of Fe(0) electrolysis. Although the O$_2$ also
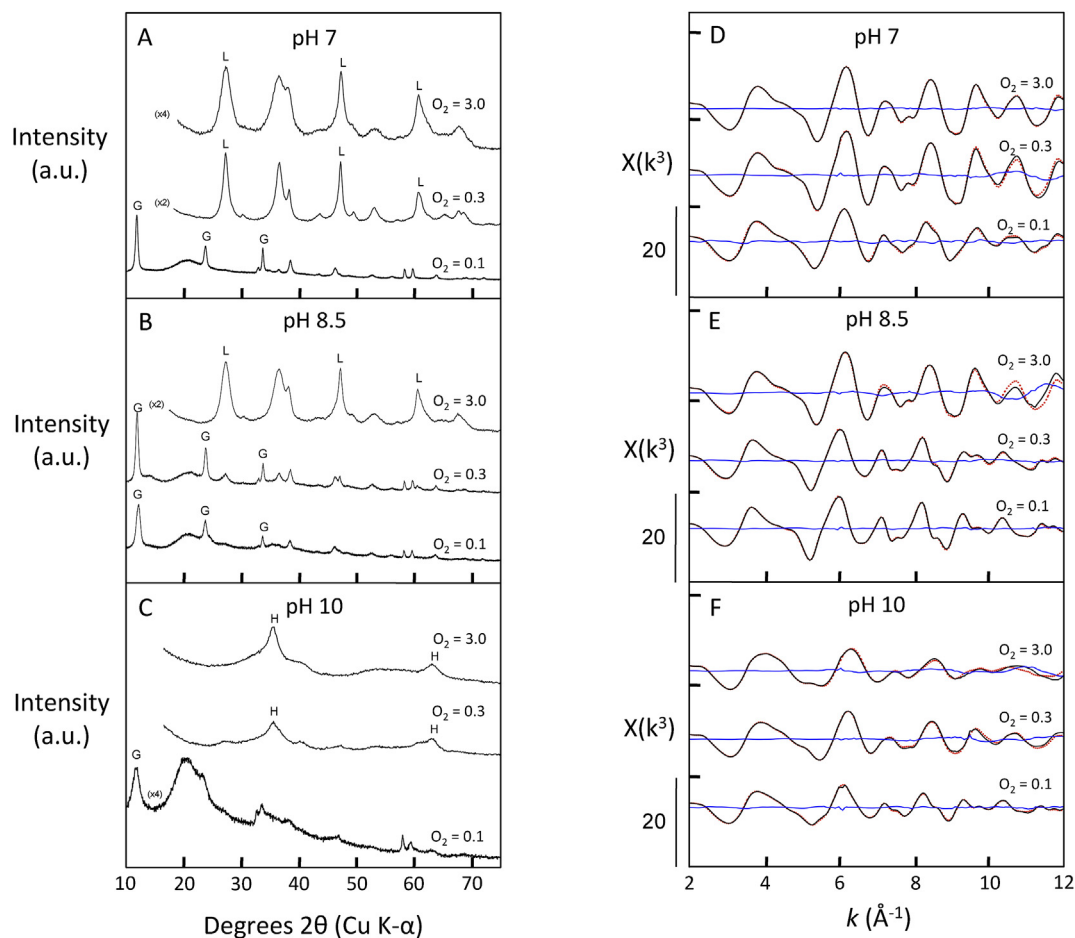
Fig. 4. XRD patterns (A—C) and Fe K-edge EXAFS spectra (D—F) of precipitates generated in carbonate solution (pH 7, 8.5 and 10) at controlled O_2 concentrations of 3.0, 0.3 and 0.1 mg L^{-1}. Major peaks in the XRD data are indicated for green rust (G), lepidocrocite (L) and hydrous ferric oxide (H). For the Fe K-edge EXAFS spectra, the black lines represent the data, the red dots represent the ITFA-derived fit and the blue lines represent the residual. The broad peak in the XRD data at 21° 2θ arises from glycerol. (For interpretation of the references to color in this figure legend, the reader is referred to the Web version of this article.)

decreased in the pH 10 sample at Fe(II) production rate $= 100\,\mu M\,min^{-1}$, it did not reach $0.1\,mg\,L^{-1}$ until the final third of the electrolysis and did not reach levels as low as in the pH 7 sample (insets in Fig. 3A). At the highest Fe(II) production rate of $300\,\mu M\,min^{-1}$, the behavior of O_2 was similar for both pH 7 and pH 10 samples, reaching $< 0.1\,mg\,L^{-1}$ within the first third of the experiment duration, where it remained until the end of the experiment. Despite the similar behavior of O_2 at pH 7 and 10, over 15% of the total Fe generated by EC remained in solution after the reaction at pH 7, whereas no Fe was detected in the filtered solution of the pH 10 sample (Table S2 in the Supplementary Data).

3.3.2. X-ray diffraction

The XRD patterns of samples generated at Fe(II) production rate $= 30\,\mu M\,min^{-1}$ in the chloride solution (Fig. 3), which were generated in the presence of O_2 levels $>3.0\,mg\,L^{-1}$, resembled those of samples produced at controlled $O_2 = 3.0\,mg\,L^{-1}$. For the pH 7 sample generated at Fe(II) production rate $= 30\,\mu M\,min^{-1}$, the XRD pattern was dominated by peaks of lepidocrocite, whereas the XRD pattern for the pH 10 sample resembled that of poorly ordered HFO. At Fe(II) production rate $= 100\,\mu M\,min^{-1}$, peaks characteristic of magnetite appeared in the XRD data for the pH 7 sample but the pH 10 sample displayed peaks primarily from lepidocrocite and HFO. The XRD data for samples generated at the highest Fe(II) production

rate of $300\,\mu M\,min^{-1}$ at pH 7 and pH 10 were both dominated by magnetite peaks. The differences in the XRD patterns of the pH 7 and pH 10 samples at the highest Fe(II) production rate were minimal, with virtually identical full width at half-maximum for the (311) peak near 36° 2θ, which indicates similar crystallite sizes. In agreement with the XRD data, transmission electron micrographs (Fig. S6 in the Supplementary Data) showed similar magnetite morphology from samples formed at pH 7 and pH 10. The particles were aggregates of up to 50 nm diameter, composed of crystallites estimated to be about 5 nm in diameter, based on the TEM images and by applying the Scherrer formula to the major (311) Bragg peak in the XRD data. Selected area electron diffraction of individual aggregates (Fig. S7 in the Supplementary Data) yielded diffraction spots expected for a single crystal, suggesting preferential orientation of magnetite grains in the aggregates, similar to that reported by Baumgartner et al. [50].

3.3.3. Iterative transformation factor analysis

The reconstructed EXAFS spectra (dotted red lines in Fig. 3E and F) of solids generated at Fe(II) production rate $= 30\,\mu M\,min^{-1}$ yielded exclusively lepidocrocite for the pH 7 sample and HFO for the pH 10 sample. At the intermediate Fe(II) production rate of $100\,\mu M\,min^{-1}$, magnetite was the dominant solid phase (>0.8) in the pH 7 sample, lepidocrocite made up the remainder, whereas the
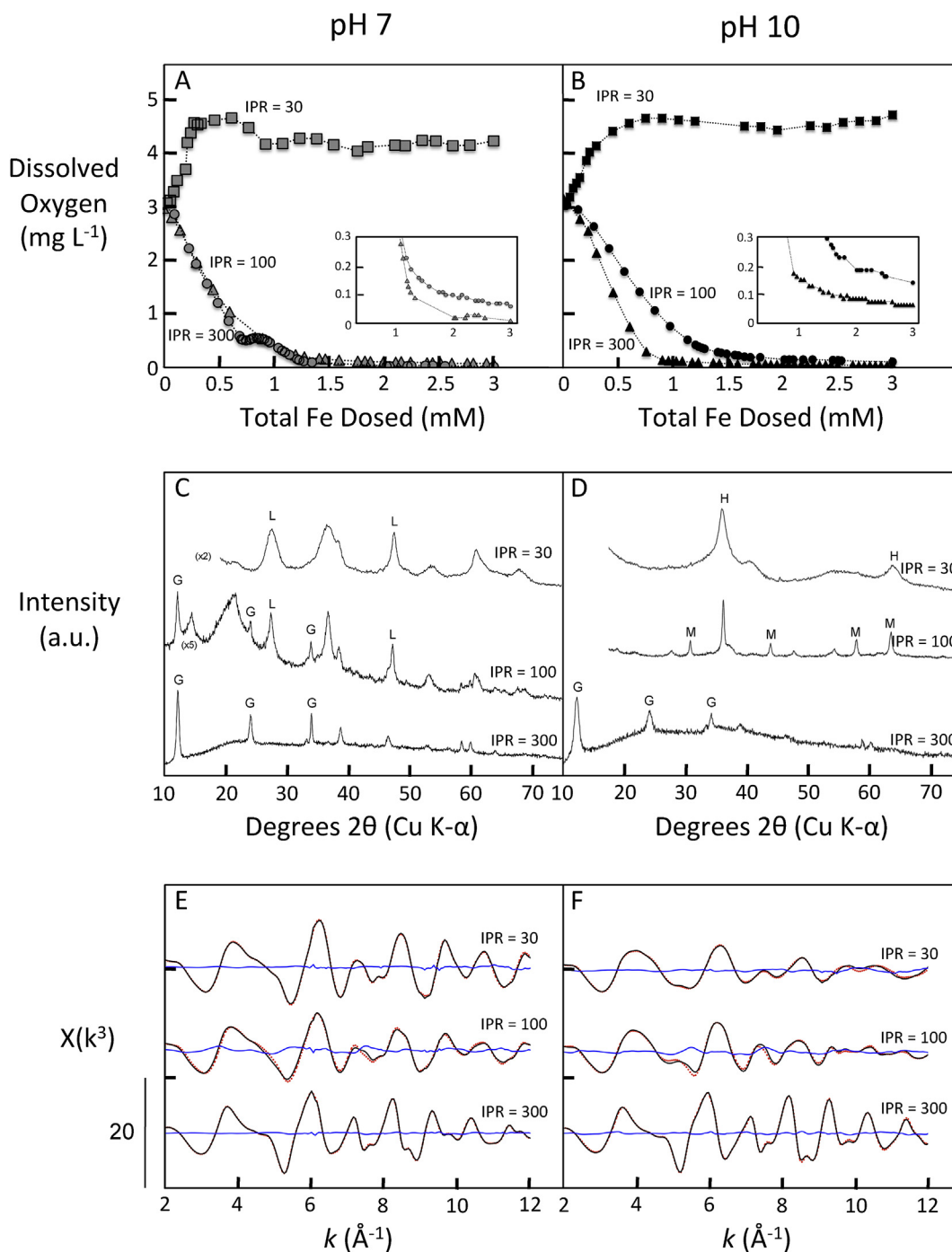
Fig. 5. Results for the O_2 drift system in the carbonate solution: dissolved oxygen measurements (A, B), XRD patterns (C, D) and Fe K-edge EXAFS spectra (E, F). The left and right columns represent experiments at pH 7 and pH 10. The total Fe dosed in A and B corresponds to a Faradaic efficiency of 1.0. Major peaks in the XRD data are indicated for green rust (G), magnetite (M), lepidocrocite (L) and hydrous ferric oxide (H). For the Fe K-edge EXAFS spectra, the black lines represent the data, the red dots represent the ITFA-derived fit and the blue lines represent the residual. The broad peak in the XRD data at 21° 2θ arises from glycerol. The Fe(II) production rate is abbreviated by IPR. (For interpretation of the references to color in this figure legend, the reader is referred to the Web version of this article.)

pH 10 sample consisted of a mixture of fractions of lepidocrocite (0.34) and HFO (0.66). The detection of magnetite for Fe(II) production rate = 100 $\mu M\,min^{-1}$ samples produced at pH 7, but not at pH 10, is consistent with the lower O_2 concentration in the pH 7 sample, which was <0.1 $mg\,L^{-1}$. At the highest Fe(II) production rate, 300 $\mu M\,min^{-1}$, the solids consisted of only magnetite, regardless of pH. No samples in the controlled O_2 or O_2 drift experiments in the chloride solution contained GR (Fig. 7).

3.4. Carbonate solution: controlled O_2 system

3.4.1. X-ray diffraction

Consistent with the X-ray diffractograms in the chloride solution, diffraction peaks for lepidocrocite dominated the pH 7 and 8.5 samples that were generated in the carbonate solution at $O_2 = 3.0\,mg\,L^{-1}$, whereas the solid from the pH 10 sample resembled poorly crystalline HFO (Fig. 4). At O_2 of 0.3 $mg\,L^{-1}$, the XRD
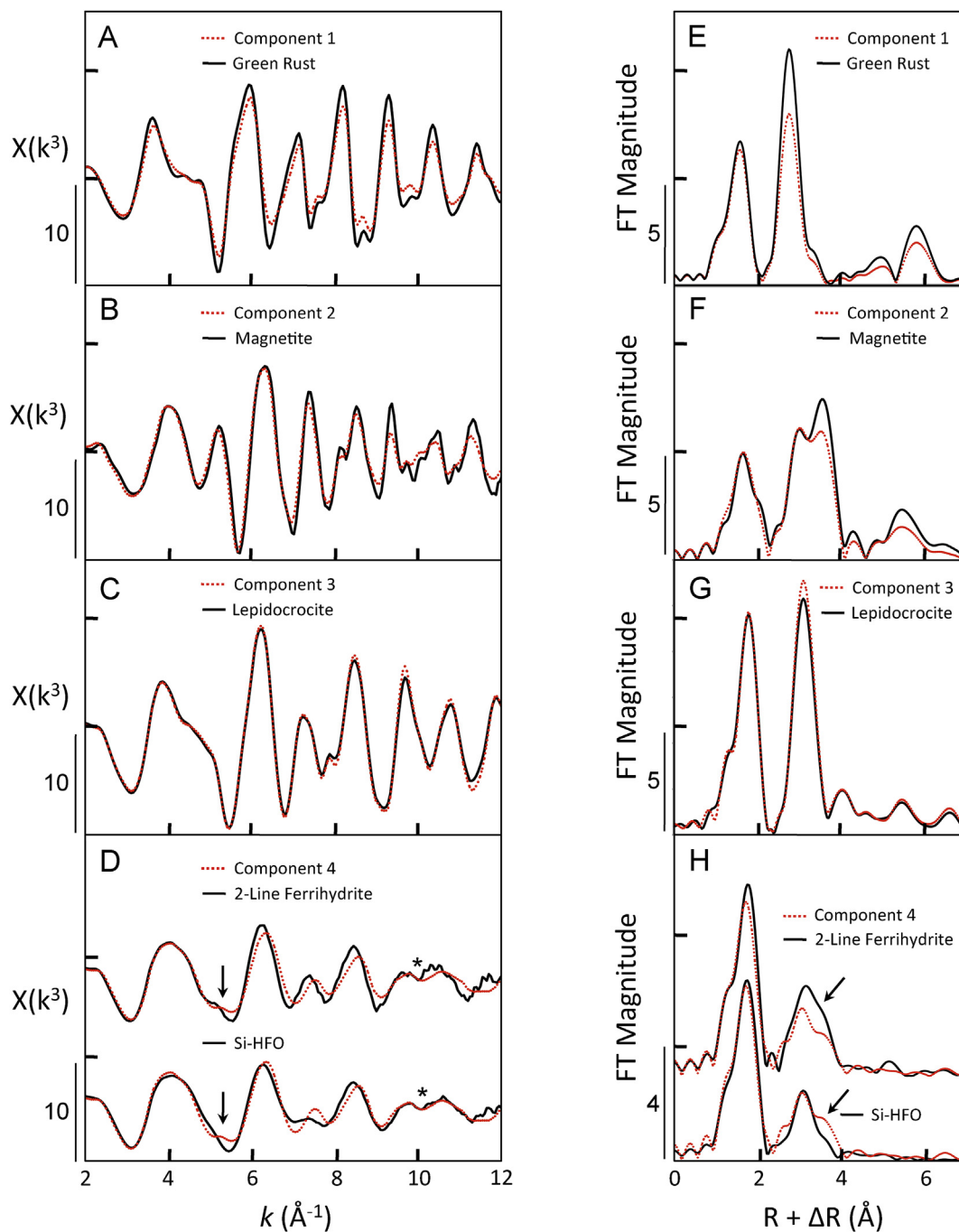
Fig. 6. Comparison between the Fe K-edge EXAFS spectra (A to D) and Fourier transforms (E to H) of ITFA extracted end member components and Fe bearing reference minerals. The solid black lines represent the reference mineral data and the dotted red lines represent the extracted components. The arrows in D and H highlight features consistent with corner sharing Fe-Fe linkages. (For interpretation of the references to color in this figure legend, the reader is referred to the Web version of this article.)

data for the pH 7 and 10 samples in the carbonate solution were similar to those at the highest O_2, 3.0 mg L^{-1}. However, the pH 8.5 sample at $O_2 = 0.3$ mg L^{-1} was dominated by peaks characteristic of carbonate green rust (GR-CO$_3$), such as the intense (003) peak near 12° 2θ and smaller (006) peak at 24° 2θ [51]. At the lowest O_2, 0.1 mg L^{-1}, XRD indicated the presence of GR-CO$_3$ in all carbonate solution samples, rather than magnetite, which had formed in the chloride solution.

3.4.2. Iterative transformation factor analysis

For precipitates generated at $O_2 = 3.0$ mg L^{-1}, lepidocrocite dominated at pH 7 (0.8) and 8.5 (1.0), whereas the pH 10 sample consisted of entirely HFO (Fig. 8). The fractions of lepidocrocite and HFO derived by ITT analysis for the samples generated at $O_2 = 3.0$ mg L^{-1} in both chloride and carbonate solution at each pH agree well (Figs. 7 and 8), which indicates that the identity of the background electrolyte ion (i.e. chloride vs carbonate) did not significantly impact the structure of the resulting Fe(III) precipitates. At O_2 of 0.3 mg L^{-1} in the carbonate solution, the fraction of lepidocrocite increased from 0.8 to 1.0 in the pH 7 sample and from 0 to 0.4 in the pH 10 sample but Fe(II,III) phases were not detected. In contrast, the EXAFS reconstruction of the sample
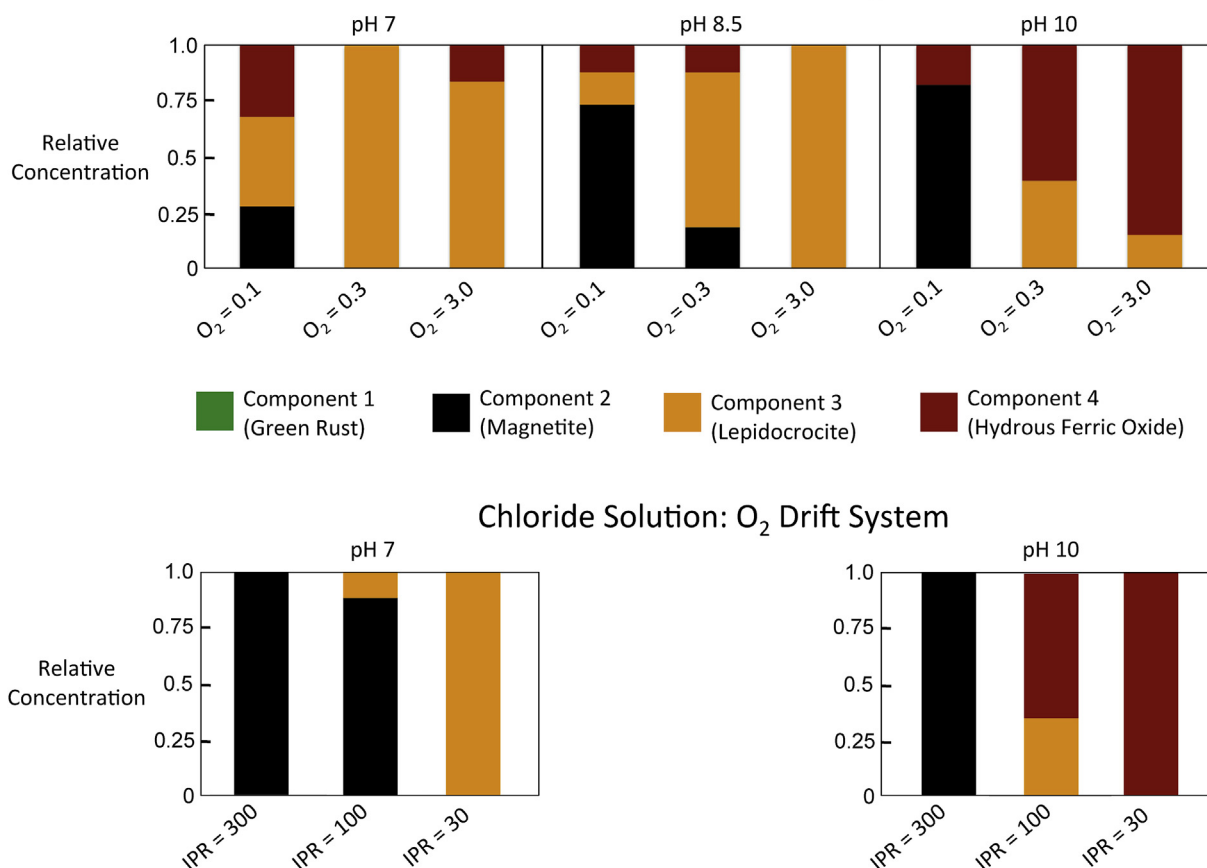
Fig. 7. ITFA derived relative concentrations of Fe bearing phases in the solids produced in the controlled O_2 and O_2 drift systems, in the chloride solution. The Fe(II) production rate is abbreviated by IPR.

produced at pH 8.5 and $O_2 = 0.3 \, mg \, L^{-1}$ yielded a GR fraction of 0.62. For precipitates generated at $O_2 = 0.1 \, mg \, L^{-1}$ in the carbonate solution, GR contributed a major fraction in the pH 8.5 sample (0.83) but was less abundant in the pH 7 (0.29) and pH 10 (0.45) samples. Although GR was not detected in any sample from the chloride solutions, magnetite was detected in the carbonate solution at a fraction of 0.2 in the pH 10 sample at $O_2 = 0.1 \, mg \, L^{-1}$.

3.5. Carbonate solution: O_2 drift system

3.5.1. Time evolution of dissolved oxygen

The behavior of O_2 during the Fe(0) EC experiments at Fe(II) production rate $= 30 \, \mu M \, min^{-1}$ in the carbonate solution was similar to that of experiments in the chloride solution. At both pH 7 and 10, the O_2 increased during Fe(0) electrolysis from 3.0 $mg \, L^{-1}$ and ended at $> 4.0 \, mg \, L^{-1}$ (Fig. 5) Consistent with the Fe(II) production rate $= 30 \, \mu M \, min^{-1}$ experiments in the chloride solution, aqueous Fe was not detected in the filtered solution of these samples (Table S2). At the intermediate Fe(II) production rate of 100 $\mu M \, min^{-1}$, the O_2 decreased to $< 0.1 \, mg \, L^{-1}$ in the pH 7 sample after the addition of $>2 \, mM$ Fe(II), whereas the O_2 decreased to $< 0.3 \, mg \, L^{-1}$ in the pH 10 sample but never reached $< 0.1 \, mg \, L^{-1}$. For experiments performed at Fe(II) production rate of 300 $\mu M \, min^{-1}$, the O_2 decreased to $< 0.1 \, mg \, L^{-1}$ after the addition of $<50\%$ of the total Fe(II) for both pH 7 and pH 10 samples. Consistent with experiments in the chloride solution, a significant percentage of the total Fe ($>25\%$) generated at pH 7 at this Fe(II) production rate remained in solution after the reaction but no residual Fe was detected at pH 10 (Table S2).

3.5.2. X-ray diffraction

The X-ray diffractograms for precipitates generated at Fe(II) production rate $= 30 \, \mu M \, min^{-1}$ in the carbonate solution only showed peaks of Fe(III) precipitates, such as lepidocrocite at pH 7 and HFO at pH 10, which is consistent with the O_2 concentration $> 3.0 \, mg \, L^{-1}$ in these experiments (Fig. 5). When the Fe(II) production rate was 100 $\mu M \, min^{-1}$, the features in the XRD pattern for the pH 7 sample indicated the presence of both lepidocrocite and GR-CO_3. However, the XRD pattern for the pH 10 sample at Fe(II) production rate $= 100 \, \mu M \, min^{-1}$ was dominated by the major Bragg diffraction peak of magnetite, positioned at $36° \, 2\theta$. At the highest Fe(II) production rate of 300 $\mu M \, min^{-1}$, intense peaks characteristic of GR-CO_3 dominated the X-ray diffractograms for both pH 7 and pH 10 samples. Peaks in the pH 10 sample, including basal plane (003) and (006) reflections, were more broad than in the pH 7 sample, indicating a GR with more structural order along the c axis formed at lower pH.

3.5.3. Iterative transformation factor analysis

The precipitates generated at Fe(II) production rate $= 30 \, \mu M \, min^{-1}$ consisted dominantly of lepidocrocite at pH 7 (0.76) and HFO at pH 10 (1.0). The reconstruction of the pH 7 sample at the intermediate Fe(II) production rate of 100 $\mu M \, min^{-1}$ showed a small fraction (<0.25) of GR, with the remaining fraction divided equally between lepidocrocite and HFO (Fig. 8). The solids produced at pH 10 and Fe(II) production rate $= 100 \, \mu M \, min^{-1}$ consisted of fractions of 0.12 GR and 0.35 magnetite, with a majority of HFO 0.53 that was not observed in the corresponding XRD pattern. Comparing the EXAFS analyses with XRD for this sample, as well as
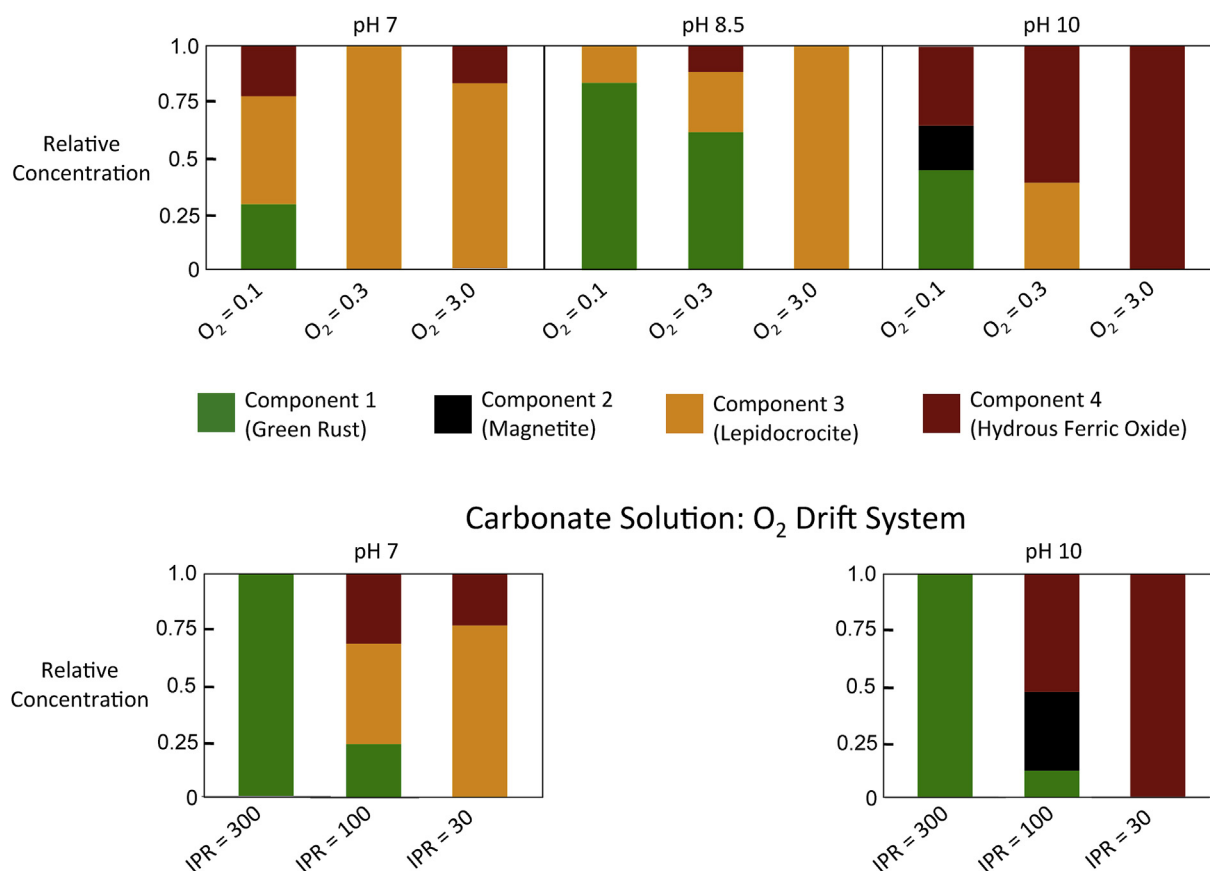
Fig. 8. Relative concentrations of Fe-bearing phases derived by ITFA for EC samples generated in the controlled O_2 and O_2 drift systems in the carbonate solution. The Fe(II) production rate is abbreviated by IPR.

others in our data set, suggests that EXAFS spectroscopy is more sensitive to poorly crystalline precipitates in solid mixtures than XRD. The composition of the pH 7 and pH 10 samples generated at Fe(II) production rate $= 300\,\mu M\,min^{-1}$ was exclusively GR (Fig. 8).

4. Discussion

4.1. Dynamics of Fe precipitation during continuous Fe(II) addition

Several processes that affect the final formation of Fe(II,III) (hydr)oxide phases occur simultaneously during Fe(0) EC. These include the continuous production of Fe(II), oxidation of Fe(II), which is coupled to O_2 consumption, Fe(III) precipitation, which then catalyzes Fe(II) oxidation, and Fe(II) mediated phase transformation. The impact of these processes can change throughout the experiment. The focus of this study was to characterize the precipitates that formed at the end of each experiment. Combining results in the controlled O_2 and O_2 drift systems with observations during the experiments provides new insight into how these co-occurring processes promote the formation of the various Fe(II,III) (hydr)oxide phases.

In the controlled O_2 system, Fe(II,III) (hydr)oxides did not form at $O_2 \geq 0.3\,mg\,L^{-1}$ at pH 7 and 10 and constituted only a fraction of the solids produced at $O_2 = 0.1\,mg\,L^{-1}$. In contrast, all O_2 drift experiments at Fe(II) production rate $= 300\,\mu M\,min^{-1}$ yielded only Fe(II,III) (hydr)oxides. Yet, in these high Fe(II) production rate experiments, the O_2 was not depleted until a significant percentage of the total Fe(II) had been added (25−50% of the total electrolysis time, Figs. 3 and 5). For example, in the carbonate solution at Fe(II) production rate $= 300\,\mu M\,min^{-1}$ and pH 7, the O_2 remained $> 0.3\,mg\,L^{-1}$ until ~1 mM Fe(II) was generated (33% of electrolysis). Based on the controlled system experiments, the solids formed at these early stages of electrolysis at Fe(II) production rate $= 300\,\mu M\,min^{-1}$ (when $O_2 > 0.1\,mg\,L^{-1}$) are expected to consist of Fe(III) precipitates, which was consistent with the beige color of the suspensions during the early stages of all experiments. However, no evidence for Fe(III) precipitates was detected in the solids at the end of the electrolysis. Therefore, our results indicate an Fe(II,III) phase formation pathway in Fe(0) EC where the continuous addition of Fe(II) consumes O_2 to $< 0.1\,mg\,L^{-1}$, forming precursory Fe(III) precipitates that are subsequently transformed to Fe(II,III) phases by aqueous Fe(II) after O_2 depletion.

The formation of Fe(II,III) (hydr)oxides by Fe(II) mediated transformation of Fe(III) precipitates has been reported previously but seldom at the rapid timescales of our experiments, i.e. minutes. For example, Hansel et al. [52] reported Fe(II) mediated transformation of ferrihydrite to magnetite over several days and GR-CO_3 has been reported to form in hours to days following Fe(II) addition to anaerobic ferrihydrite suspensions [53,54]. A critical factor determining the extent of Fe(II) mediated transformation of Fe(III) precursors at $pH \geq 7$ is the amount of Fe(II) added. Yang et al. [55], reported that goethite formed during addition of 0.36 mM $FeSO_4$ to anaerobic reactors containing ferrihydrite, whereas $FeSO_4$ additions of >1.8 mM were required to produce Fe(II,III) (hydr)oxide minerals. The importance of adding substantial Fe(II) after O_2 depletion to form Fe(II,III) (hydr)oxides by Fe(0) EC is reflected in our experiments at Fe(II) production rate $= 100\,\mu M\,min^{-1}$ in the carbonate solution at pH 7. For this experiment, the solids

contained only a small fraction of Fe(II,III) (hydr)oxides despite a final $O_2 < 0.1\,mg\,L^{-1}$, which was likely related to insufficient Fe(II) (<1 mM) concentrations added after O_2 depletion (Fig. 5).

Following our proposed Fe(II,III) (hydr)oxide formation pathway, Fe(II,III) phases would be favored when the flux of Fe(II) is sufficient to rapidly decrease the O_2 and provide enough Fe(II) to transform precursory Fe(III) precipitates. Therefore, the requisite Fe(II) flux leading to Fe(II,III) phases also depends on the rate of O_2 replenishment by O_2 from air. Measurements of the rate of O_2 increase in our experiments in the absence of applied current revealed an O_2 influx of ~30 μM O_2 min^{-1} at $O_2 = 0.5\,mg\,L^{-1}$ (Supplementary Data, Fig. S8). Because Fe(II,III) phases were detected in the Fe(II) production rate = 100 μM min^{-1} experiments, with the highest fraction of these phases detected at Fe(II) production rate = 300 μM min^{-1}, we conclude that Fe(II,III) (hydr)oxide formation in Fe(0) EC, and natural systems by extension, can occur when the Fe(II) flux is at least 3 times greater than the rate of O_2 regeneration, with an Fe(II) flux 10 times greater leading to the predominance of Fe(II,III) (hydr)oxides. Finally, it is important to note that the Fe(II) flux and total Fe(II) concentration required to decrease $O_2 < 0.1\,mg\,L^{-1}$, and therefore produce Fe(II,III) phases, depends on the initial O_2 concentration. For experiments at Fe(II) production rate = 300 μM min^{-1}, the O_2 decreased at a ratio of ~5 mg O_2 per mmol Fe(II) added. This suggests that ~2 mM Fe(II) would be required to deplete O_2 in an air saturated solution under our experimental conditions. However, significantly less Fe(II) is likely required to deplete O_2 if the O_2 influx is minimal.

4.2. Impact of pH and electrolyte type on Fe(II,III) (hydr)oxide formation

4.2.1. Background electrolyte

While the Fe(II) production rate and O_2 controlled the formation of Fe(II,III) versus Fe(III) precipitates, the ionic composition of the background electrolyte determined the type of Fe(II,III) precipitate. In both controlled O_2 and O_2 drift systems, magnetite was the dominant Fe(II,III) phase formed in the presence of chloride, whereas GR-CO$_3$ was generally favored in carbonate solution, in agreement with our hypotheses. Even at carbonate concentrations as low as 0.5 mM (carbonate to iron molar ratio of 0.166), magnetite formation was kinetically outcompeted by GR-CO$_3$ formation (Supplementary Data, Fig. S9), which reveals the importance of excluding carbonate if magnetite is the desired phase to form at the timescales of our experiments. The absence of GR-Cl in the chloride solution and the inhibition of magnetite in most of the carbonate solution experiments is strong evidence for the preference for GR when carbonate occupies the interlayer relative to chloride, which has been proposed in previous work [2,31]. These observations can be explained by the enhanced stabilization of positively charged brucite like Fe(II)/Fe(III) octahedral sheets by the more negatively charged carbonate ion compared with chloride [31].

Despite different ideal Fe(II):Fe(III) ratios of 0.5 for magnetite and 2.0 for GR-CO$_3$ [56,57], the fractions of the two types of Fe(II,III) (hydr)oxides in the solid phase were generally similar for a given pH and controlled O_2 concentration. For example, at pH 7 and $O_2 = 0.1\,mg\,L^{-1}$, the fractions of magnetite (0.28, chloride solution) and GR-CO$_3$ (0.29, carbonate solution) were nearly identical (Figs. 7 and 8). Exceptions to this trend were the pH 10 experiments, where a fraction of magnetite formed in the carbonate solution, which is consistent with the narrowing stability field of GR as pH increases (Fig. 1) and has been reported in previous work [58]. However, our experiments were performed over rapid time scales, i.e. 10–100 min, and the solid phase was prepared for characterization immediately at the end of the experiment. Because GR phases are metastable [29,59,60], structural transformation of GR to magnetite

during aging periods longer than the 10 min reaction time of our experiments can occur, controlled by the thermodynamic stability of magnetite [61]. This is the subject of our ongoing work.

4.2.2. Solution pH

Relative to other (electro)chemical variables (i.e. Fe(II) production rate, O_2, ionic composition), solution pH played a secondary role in the formation and structure of EC-generated Fe(II,III) (hydr)oxides. Higher fractions of Fe(II,III) (hydr)oxides formed in controlled O_2 experiments at pH 10 relative to pH 7, with magnetite detected only at pH 10 in the carbonate solution (Fig. 8). The formation of small fractions of Fe(II,III) phases at $O_2 = 0.3\,mg\,L^{-1}$ in both chloride and carbonate solutions at pH 8.5, but not at pH 7 and 10, implies an optimum pH for magnetite and GR-CO$_3$ formation in these experiments near 8 to 9.

Although the fraction of magnetite and GR-CO$_3$ derived by EXAFS analysis was independent of pH for solids generated at Fe(II) production rate = 300 μM min^{-1}, solution pH did impact other important properties for these samples. For example, the amount of aqueous Fe measured at the end of the Fe(II) production rate = 300 μM min^{-1} experiments was a significant fraction of the total Fe in both the chloride (~0.2) and carbonate solutions (~0.3) at pH 7. The aqueous Fe remaining at the end of electrolysis was <1% of the total Fe added for all experiments performed at pH 8.5 and 10, regardless of the O_2 concentration, which is consistent with the strong decrease in solubility with increasing pH of magnetite [28] and GR-CO$_3$ [29]. The persistence of aqueous Fe remaining after Fe(II,III) (hydr)oxide production is an important consideration for Fe(0) EC field treatment and should be avoided because i) electricity is spent to generate Fe(II) that does not contribute to particle formation and therefore contaminant removal and ii) residual Fe(II) can oxidize after the particle separation stage of treatment, negatively impacting product water aesthetics.

The minor role of pH on the formation and structure of EC generated Fe(II,III) (hydr)oxides contrasts the strong impact of pH when only Fe(III) phases formed. Across all experiments that produced only Fe(III) precipitates, the formation of lepidocrocite was favored at pH 7, whereas poorly ordered HFO formed at pH 10. These results can be explained by a similar Fe(II) mediated Fe(III) precipitate transformation reaction as described above for Fe(II,III) phase formation but with lower aqueous Fe(II) concentrations. As pH increased from 7 to 10, the rate of Fe(II) oxidation by O_2 increased several orders of magnitude, leading to virtually instantaneous Fe(II) oxidation by O_2 [30]. Therefore, in experiments performed at pH 10 and $O_2 \geq 3.0\,mg\,L^{-1}$, EC-generated aqueous Fe(II) oxidizes rapidly, leading to only HFO precursor phases. In contrast, at pH 7, the lifetime of Fe(II) is sufficient to mediate the crystallization of fresh Fe(III) precipitates to form lepidocrocite, consistent with previous work [52,62,63].

4.3. Implications for engineered and natural systems

4.3.1. Fe(II,III) (hydr)oxide production in Fe(0) EC field systems

The selective generation of Fe(II,III) (hydr)oxides can improve Fe(0) EC system performance in several ways, such as facilitating low cost particle removal (i.e. magnetic separation) or by detoxifying contaminated waters by reductive transformation of target species (e.g. U(VI), Se(VI), nitrate, organic solvents) [1–3,64,65]. The Fe(II,III) (hydr)oxide formation conditions derived from our work, i.e. Fe(II) production rate $\geq$ 10 times higher than O_2 influx, indicate that these minerals can be generated readily during Fe(0) EC field treatment by modifying system design to minimize air to water exchange. This simple approach can include: i) avoiding mixing conditions that induce turbulence in reactors open to the atmosphere, ii) altering reactor shape to decrease the ratio of exposed

solution area to solution volume or iii) fashioning a lid for the reactor. The impact of the first two modifications (i.e. mixing rate and reactor geometry) on O_2 influx in our experiments are provided in the Supplementary Data (Fig. S8) to highlight their importance.

Another option is to use an independent Fe(II) dosing chamber that is separated from the source water influent. This scheme is attractive because properties of the electrolyte solution, including O_2, pH and ionic composition, can be controlled in a small, separate dosing chamber, effectively and at low cost, to yield the desired Fe(II,III) (hydr)oxide. Using locally available chemicals (small volume of distilled or deionized water and NaCl or $NaHCO_3$), the electrolyte composition could be altered to selectively generate magnetite for its enhanced sorption reactivity with oxyanions and magnetic properties [10] or GR-CO_3 for its ability to reductively degrade contaminants [31], which would otherwise be constrained by the natural composition of the influent solution. In addition, the solution pH could be adjusted to >7 more practically in this independent chamber, which would minimize undesirable aqueous Fe remaining after Fe(II,III) (hydr)oxide formation. The Fe(II,III) (hydr)oxides produced on-site in this design can subsequently be concentrated and harvested directly from the dosing chamber and transported to a larger reaction tank receiving contaminated source water. This option prevents the aggregation and subsequent loss of reactivity of nanoscale Fe(II,III) (hydr)oxides as a result of drying, a major drawback of offsite nanoparticle production [66,67].

4.3.2. Pathways of Fe(II,III) (hydr)oxide formation in the environment

Iron precipitation at the interface of oxic and suboxic conditions is a widespread phenomenon in redox-stratified environments. This process exerts a major influence on the geochemical cycling of nutrients and trace contaminants, with nutrient and contaminant uptake strongly dependent on Fe precipitate structure [48,68]. Our experimental system based on Fe(0) electrolysis permitted precise control of the Fe(II) flux, which mimics a redox boundary, and allowed us to determine for the first time the interplay between the initial O_2, the O_2 influx and the rate of Fe(II) addition that leads to Fe(II,III) (hydr)oxide formation. The highest fraction of Fe(II,III) precipitates formed when more than half of the total 3 mM Fe(II) was added after O_2 was depleted (i.e. $O_2 < 0.1$ mg L^{-1}), which occurred when the Fe(II) flux was ≥ 10 times higher than the O_2 influx. Under these conditions, magnetite and GR formation proceeds through a pathway where Fe(II) addition transforms precursory Fe(III) precipitates in rapid times scales of <10 min. Our work suggests that this Fe(II)-mediated transformation pathway could be a major pathway for Fe(II,III) (hydr)oxide formation in Fe rich marine and terrestrial environments prone to abrupt spatial or temporal transitions in redox conditions. This rapid formation pathway is particularly relevant for biotically mediated formation of Fe(II,III) (hydr)oxides in light of the high fluxes of Fe(II) produced by iron reducing bacteria [69]. Finally, although magnetite is favored over GR thermodynamically [56,61], GR-CO_3 outcompeted magnetite kinetically in our experiments in the carbonate solution experiments. Dissolved inorganic carbon is ubiquitous in the environment and our results indicate that its presence at carbonate to iron ratios >0.167 (or carbonate to chloride ratios > 0.05) would favor GR-CO_3 formation initially. This contrasts the greater abundance of magnetite relative to GRs often reported for groundwaters, soils and sediments [70,71]. Therefore, the persistence of GR in our experiments and not in natural systems suggests that GR is a metastable Fe(II,III) phase during Fe(II) mediated Fe(III) precipitate transformation, which has been proposed in relation to the biogenic transformation of lepidocrocite to magnetite [72]. Another explanation of the natural abundance of magnetite relative to GR could be that microenvironments created during biogenic Fe(II,III)

(hydr)oxide formation inhibit the interaction of dissolved inorganic carbon with the precipitating phase.

5. Conclusions

The formation of Fe(II,III) (hydr)oxides by Fe(0) electrolysis depended on the initial O_2 concentration and the balance between the influx of Fe(II) and O_2. In the Fe(0) EC system, the interplay among these variables can be controlled to selectively generate Fe(II,III) phases by ensuring a ten fold higher Fe(II) production rate relative to O_2 influx, which can be achieved by increasing the applied current or by minimizing O_2 influx to the reactor. At Fe(II) to O_2 molar flux ratios ≥ 10, the continuous addition of Fe(II) was sufficient to consume O_2 to < 0.1 mg L^{-1}, forming precursor Fe(III) precipitates, which were transformed to Fe(II,III) (hydr)oxides by Fe(II) added subsequently. The composition of the electrolyte solution controlled the type of Fe(II,III) (hydr)oxide: magnetite formed in chloride solutions and GR-CO_3 formed in carbonate solutions. GR-Cl did not form in the chloride solutions but a small fraction of magnetite formed in some carbonate solutions at pH 10. Solution pH played a secondary role in the formation of Fe(II,III) (hydr)oxides but largely determined the amount of aqueous Fe remaining after Fe(II,III) phase formation. Our study helps to constrain the conditions of Fe(II,III) (hydr)oxide formation in the environment and provides useful information for improving the design of remediation strategies based on the production of Fe(II,III) (hydr)oxides.

Appendix A. Supplementary data

Supplementary data related to this article can be found at https://doi.org/10.1016/j.electacta.2018.08.031.

References

[1] E. O'Loughlin, D. Burris, Reduction of halogenated ethanes by green rust, Environ. Toxicol. Chem. 23 (2004) 41–48.

[2] H. Hansen, S. Guldberg, M. Erbs, C. Koch, Kinetics of nitrate reduction by green rusts - effects of interlayer anion and Fe(II): Fe(III) ratio, Appl. Clay Sci. 18 (2001) 81–91.

[3] M. Elsner, R. Schwarzenbach, S. Haderlein, Reactivity of Fe(II)-bearing minerals toward reductive transformation of organic contaminants, Environ. Sci. Technol. 38 (2004) 799–807.

[4] L. Skovbjerg, S. Stipp, S. Utsunomiya, R. Ewing, The mechanisms of reduction of hexavalent chromium by green rust sodium sulphate: formation of Cr-goethite, Geochim. Cosmochim. Acta 70 (2006) 3582–3592.

[5] Y.H. Wang, G. Morin, G. Ona-Nguema, F. Juillot, F. Guyot, G. Calas, G.E. Brown, Evidence for different surface speciation of arsenite and arsenate on green rust: an EXAFS and XANES study, Environ. Sci. Technol. 44 (2010) 109–115.

[6] S.R. Randall, D.M. Sherman, K.V. Ragnarsdottir, Sorption of As(V) on green rust (Fe-4(II)Fe-2(III)(OH)(12)SO4 center dot 3H(2)O) and lepidocrocite (gamma-FeOOH): surface complexes from EXAFS spectroscopy, Geochim. Cosmochim. Acta 65 (2001) 1015–1023.

[7] Y. Wang, G. Morin, G. Ona-Nguema, G. Brown, Arsenic(III) and arsenic(V) speciation during transformation of lepidocrocite to magnetite, Environ. Sci. Technol. 48 (2014) 14282–14290.

[8] Y. Wang, G. Morin, G. Ona-Nguema, F. Juillot, G. Calas, G. Brown, Distinctive arsenic(V) trapping modes by magnetite nanoparticles induced by different sorption processes, Environ. Sci. Technol. 45 (2011) 7258–7266.

[9] G. Morin, Y. Wang, G. Ona-Nguema, F. Juillot, G. Calas, N. Menguy, E. Aubry, J. Bargar, G. Brown, EXAFS and HRTEM evidence for as(III)-containing surface precipitates on nanocrystalline magnetite: implications for as sequestration, Langmuir 25 (2009) 9119–9128.

[10] C. Yavuz, J. Mayo, W. Yu, A. Prakash, J. Falkner, S. Yean, L. Cong, H. Shipley, A. Kan, M. Tomson, D. Natelson, V. Colvin, Low-field magnetic separation of monodisperse Fe3O4 nanocrystals, Science 314 (2006) 964–967.

[11] G. Unsoy, U. Gunduz, O. Oprea, D. Ficai, M. Sonmez, M. Radulescu, M. Alexie, A. Ficai, Magnetite: from synthesis to applications, Curr. Top. Med. Chem. 15 (2015) 1622–1640.

[12] C. Bhave, S. Shejwalkar, A review on the synthesis and applications of green rust for environmental pollutant remediation, Int. J. Environ. Sci. Technol. 15 (6) (2017) 1243–1248.

[15] L. Legrand, M. Abdelmoula, A. Gehin, A. Chausse, J. Genin, Electrochemical formation of a new Fe(II)-Fe(III) hydroxy-carbonate green rust: characterisation and morphology, Electrochim. Acta 46 (2001) 1815–1822.

[16] J. Gomes, A. Baksi, I. Haider, J. Gossage, H. Moreno, D. Cocke, Electrochemical generation of green rust and modified green rust for water treatment applications, Curr. Inorg. Chem. 6 (2016) 83–91.

[17] C. Tsouris, D. DePaoli, J. Shor, M. Hu, T. Ying, Electrocoagulation for magnetic seeding of colloidal particles, Colloid. Surf. Physicochem. Eng. Aspects 177 (2001) 223–233.

[18] P. Holt, G. Barton, C. Mitchell, The future for electrocoagulation as a localised water treatment technology, Chemosphere 59 (2005) 355–367.

[19] S.E. Amrose, S.R.S. Bandaru, C. Delaire, C.M. van Genuchten, A. Dutta, A. DebSarkar, C. Orr, J. Roy, A. Das, A.J. Gadgil, Electro-chemical arsenic remediation: field trials in West Bengal, Sci. Total Environ. 488–489 (2014) 539–546.

[20] C. Delaire, C.M. van Genuchten, K.L. Nelson, S.E. Amrose, A.J. Gadgil, E. coli attenuation by Fe electrocoagulation in synthetic bengal groundwater: effect of pH and natural organic matter, Environ. Sci. Technol. 49 (2015) 9945–9953.

[21] C. Pan, L. Troyer, J. Catalano, D. Giammar, Dynamics of chromium(VI) removal from drinking water by iron electrocoagulation, Environ. Sci. Technol. 50 (2016) 13502–13510.

[22] USEPA, CURE Electrocoagulation Technology, Innovative Technology Evaluation Report, National Risk Management Research, Laboratory Office of Research and Development, 1998.

[23] D. Lakshmanan, D.A. Clifford, G. Samanta, Ferrous and ferric ion generation during iron electrocoagulation, Environ. Sci. Technol. 43 (2009) 3853–3859.

[24] J.A.G. Gomes, P. Daida, M. Kesmez, M. Weir, H. Moreno, J.R. Parga, G. Irwin, H. McWhinney, T. Grady, E. Peterson, D.L. Cocke, Arsenic removal by electrocoagulation using combined Al-Fe electrode system and characterization of products, J. Hazard. Mater. 139 (2007) 220–231.

[25] Y. Weng, L. Rusakova, A. Baikalov, J. Chen, N. Wu, Microstructural evolution of nanocrystalline magnetite synthesized by electrocoagulation, J. Mater. Res. 20 (2005) 75–80.

[26] K. Dubrawski, M. Mohseni, In-situ identification of iron electrocoagulation speciation and application for natural organic matter (NOM) removal, Water Res. 47 (2013) 5371–5380.

[27] L. Li, C.M. van Genuchten, S.E.A. Addy, J. Yao, N. Gao, A.J. Gadgil, Modeling As(III) oxidation and removal with iron electrocoagulation in groundwater, Environ. Sci. Technol. 46 (2012) 12038–12045.

[28] P. Tremaine, J. LeBlanc, The solubility of magnetite and the hydrolysis and oxidation of Fe2+ in water to 300-degrees-C, J. Solut. Chem. 9 (1980) 415–442.

[29] R. Guilbaud, M. White, S. Poulton, Surface charge and growth of sulphate and carbonate green rust in aqueous media, Geochim. Cosmochim. Acta 108 (2013) 141–153.

[30] W. Stumm, G. Lee, Oxygenation of ferrous iron, Ind. Eng. Chem. 53 (1961) 143–146.

[31] H. Hansen, Environmental chemistry of iron(II)-iron(III) LDHs (green rusts), in: V. Rives (Ed.), Layered Double Hydroxides: Present and Future, Nova Science Publishers, 2001.

[32] C. van Genuchten, K. Dalby, M. Ceccato, S. Stipp, K. Dideriksen, Factors affecting the Faradaic efficiency of Fe(0) electrocoagulation, J. Environ. Chem. Eng. 5 (5) (2017) 4958–4968.

[33] R.M. Cornell, U. Schwertmann, The Iron Oxides : Structure, Properties, Reactions, Occurrence, and Uses, VCH, Weinheim ; New York, 1996.

[34] C.M. van Genuchten, J. Pena, S.E. Amrose, A.J. Gadgil, Structure of Fe(III) precipitates generated by the electrolytic dissolution of Fe(0) in the presence of groundwater ions, Geochim. Cosmochim. Acta 127 (2014) 285–304.

[35] J.M.R. Genin, G. Bourrie, F. Trolard, M. Abdelmoula, A. Jaffrezic, P. Refait, V. Maitre, B. Humbert, A. Herbillon, Thermodynamic equilibria in aqueous suspensions of synthetic and natural Fe(II)-Fe(III) green rusts: occurrences of the mineral in hydromorphic soils, Environ. Sci. Technol. 32 (1998) 1058–1068.

[36] Y. Zheng, M. Stute, A. van Geen, I. Gavrieli, R. Dhar, H. Simpson, P. Schlosser, K. Ahmed, Redox control of arsenic mobilization in Bangladesh groundwater, Appl. Geochem. 19 (2004) 201–214.

[37] S.E. Amrose, Z. Burt, I. Ray, Safe drinking water for low-income regions, Annu. Rev. Environ. Resour. 40 (2015) 203–231.

[38] H. Hansen, Composition, stabilization, and light-absorption of Fe(II)Fe(III) hydroxy-carbonate (Green Rust), Clay Miner. 24 (1989) 663–669.

[39] S.D. Kelly, D. Hesterberg, B. Ravel, Analysis of soils and minerals using X-ray absorption spectroscopy, in: Methods of Soil Analysis. Part 5. Mineralogical Methods, 2008. SSA Book Series No.5.

[40] M. Borsboom, W. Bras, I. Cerjak, D. Detollenaere, D. van Loon, P. Goedtkindt, M. Konijnenburg, P. Lassing, Y. Levine, B. Munneke, M. Oversluizen, R. van Tol, E. Vlieg, The Dutch-Belgian beamline at the ESRF, J. Synchrotron Radiat. 5 (1998) 518–520.

[41] S. Nikitenko, A. Beale, A. van der Eerden, S. Jacques, O. Leynaud, M. O'Brien, D. Detollenaere, R. Kaptein, B. Weckhuysen, W. Bras, Implementation of a combined SAXS/WAXS/QEXAFS set-up for time-resolved in situ experiments, J. Synchrotron Radiat. 15 (2008) 632–640.

[42] S. Webb, SIXPACK: a graphical user interface for XAS analysis using IFEFFIT, Phys. Scr. T115 (2005) 1011–1014.

[43] C. van Genuchten, S. Addy, J. Pena, A. Gadgil, Removing arsenic from synthetic groundwater with iron electrocoagulation: an Fe and as K-edge EXAFS study, Environ. Sci. Technol. 46 (2012) 986–994.

[44] A. Rossberg, T. Reich, G. Bernhard, Complexation of uranium(VI) with protocatechuic acid - application of iterative transformation factor analysis to EXAFS spectroscopy, Anal. Bioanal. Chem. 376 (2003) 631–638.

[45] C. Lenz, T. Behrends, T. Jilbert, M. Silveira, C.P. Slomp, Redox-dependent changes in manganese speciation in baltic sea sediments from the holocene thermal maximum: an EXAFS, XANES and LA-ICP-MS study, Chem. Geol. 370 (2014) 49–57.

[46] A. Rossberg, K. Ulrich, S. Weiss, S. Tsushima, T. Hiemstra, A. Scheinost, Identification of uranyl surface complexes an ferrihydrite: advanced EXAFS data analysis and CD-MUSIC modeling, Environ. Sci. Technol. 43 (2009) 1400–1406.

[47] F. Trolard, G. Bourrie, M. Abdelmoula, P. Refait, F. Feder, Fougerite, a new mineral of the pyroaurite-iowaite group: description and crystal structure, Clay Clay Miner. 55 (2007) 323–334.

[48] A. Voegelin, R. Kaegi, J. Frommer, D. Vantelon, S.J. Hug, Effect of phosphate, silicate, and Ca on Fe(III)-precipitates formed in aerated Fe(II)- and As(III)-containing water studied by X-ray absorption spectroscopy, Geochim. Cosmochim. Acta 74 (2010) 164–186.

[49] G.S. Pokrovski, J. Schott, F. Garges, J.L. Hazemann, Iron (III)-silica interactions in aqueous solution: insights from X-ray absorption fine structure spectroscopy, Geochim. Cosmochim. Acta 67 (2003) 3559–3573.

[50] J. Baumgartner, A. Dey, P. Bomans, C. Le Coadou, P. Fratzl, N. Sommerdijk, D. Faivre, Nucleation and growth of magnetite from solution, Nat. Mater. 12 (2013) 310–314.

[51] M. Abdelmoula, P. Refait, S. Drissi, J. Mihe, J. Genin, Conversion electron Mossbauer spectroscopy and X-ray diffraction studies of the formation of carbonate-containing green rust one by corrosion metallic iron in NaHCO3 and (NaHCO3+NaC1) solutions, Corrosion Sci. 38 (1996) 623–633.

[52] C. Hansel, S. Benner, S. Fendorf, Competing Fe(II)-induced mineralization pathways of ferrihydrite, Environ. Sci. Technol. 39 (2005) 7147–7153.

[53] M. Usman, K. Hanna, M. Abdelmoula, A. Zegeye, P. Faure, C. Ruby, Formation of green rust via mineralogical transformation of ferric oxides (ferrihydrite, goethite and hematite), Appl. Clay Sci. 64 (2012) 38–43.

[54] A. Sumoondur, S. Shaw, I. Ahmed, L. Benning, Green rust as a precursor for magnetite: an in situ synchrotron based study, Mineral. Mag. 72 (2008) 201–204.

[55] L. Yang, C. Steefel, M. Marcus, J. Bargar, Kinetics of Fe(II)-Catalyzed transformation of 6-line ferrihydrite under anaerobic flow conditions, Environ. Sci. Technol. 44 (2010) 5469–5475.

[56] S.H. Drissi, P. Refait, M. Abdelmoula, J.M.R. Genin, The preparation and thermodynamic properties of Fe(II)-Fe(III) hydroxide-carbonate (Green-Rust-1) - pourbaix diagram of iron in carbonate-containing aqueous media, Corrosion Sci. 37 (1995) 2025–2041.

[57] W. Bragg, The structure of magnetite and the spinels, Nature 95 (1915), 561-561.

[58] K.L. Dubrawski, C.M. van Genuchten, C. Delaire, S.E. Amrose, A.J. Gadgil, M. Mohseni, Production and transformation of mixed-valent nanoparticles generated by Fe(0) electrocoagulation, Environ. Sci. Technol. 49 (2015) 2171–2179.

[59] X. Feng, X. Wang, M. Zhu, L. Koopal, H. Xu, Y. Wang, F. Liu, Effects of phosphate and silicate on the transformation of hydroxycarbonate green rust to ferric oxyhydroxides, Geochim. Cosmochim. Acta 171 (2015) 1–14.

[60] O. Benali, M. Abdelmoula, P. Refait, J. Genin, Effect of orthophosphate on the oxidation products of Fe(II)-Fe(III) hydroxycarbonate: the transformation of green rust to ferrihydrite, Geochim. Cosmochim. Acta 65 (2001) 1715–1726.

[61] R. Robie, B. Hemingway, Thermodynamic properties of minerals and related substances at 298.15 K and 1 bar (10⁵ pascals) pressure and at higher temperatures, U. S. Geol. Surv. Bull. 2131 (1995) 461.

[62] D. Boland, R. Collins, C. Miller, C. Glover, T. Waite, Effect of solution and solid-phase conditions on the Fe(II)-Accelerated transformation of ferrihydrite to lepidocrocite and goethite, Environ. Sci. Technol. 48 (2014) 5477–5485.

[63] H. Pedersen, D. Postma, R. Jakobsen, O. Larsen, Fast transformation of iron oxyhydroxides by the catalytic action of aqueous Fe(II), Geochim. Cosmochim. Acta 69 (2005) 3967–3977.

[64] P. Refait, L. Simon, J.M.R. Genin, Reduction of SeO42- anions and anoxic

formation of iron(II)-iron(III) hydroxy selenate green rust, Environ. Sci. Technol. 34 (2000) 819–825.

[65] E. O'Loughlin, S. Kelly, R. Cook, R. Csencsits, K. Kemner, Reduction of Uranium(VI) by mixed iron(II/iron(III) hydroxide (green rust): formation of UO2 nanoparticles, Environ. Sci. Technol. 37 (2003) 721–727.

[66] S. Ghosh, W. Jiang, D. McClements, B. Xing, Colloidal stability of magnetic iron oxide nanoparticles: influence of natural organic matter and synthetic polyelectrolytes, Langmuir 27 (2011) 8036–8043.

[67] R. Joseyphus, K. Shinoda, D. Kodama, B. Jeyadevan, Size controlled Fe nanoparticles through polyol process and their magnetic properties, Mater. Chem. Phys. 123 (2010) 487–493.

[68] M. Usman, K. Hanna, M. Abdelmoula, C. Ruby, Magnetite formation via Fe-II induced mineralogical transformations of ferric oxyhydroxides, Geochim. Cosmochim. Acta 74 (2010). A1067-A1067.

[69] E. Roden, M. Urrutia, Influence of biogenic Fe(II) on bacterial crystalline Fe(III) oxide reduction, Geomicrobiol. J. 19 (2002) 209–251.

[70] Y. Pan, N. Petersen, A. Davila, L. Zhang, M. Winklhofer, Q. Liu, M. Hanzlik, R. Zhu, The detection of bacterial magnetite in recent sediments of Lake Chiemsee (southern Germany), Earth Planet. Sci. Lett. 232 (2005) 109–123.

[71] D. Cummings, A. March, B. Bostick, S. Spring, F. Caccavo, S. Fendorf, R. Rosenzweig, Evidence for microbial Fe(III) reduction in anoxic, mining-impacted lake sediments (Lake Coeur d'Alene, Idaho), Appl. Environ. Microbiol. 66 (2000) 154–162.

[72] G. Ona-Nguema, M. Abdelmoula, F. Jorand, O. Benali, A. Gehin, J. Block, J. Genin, Iron(II,III) hydroxycarbonate green rust formation and stabilization from lepidocrocite bioreduction, Environ. Sci. Technol. 36 (2002) 16–20.

[73] W. Feitknecht, P. Schindler, Solubility constant of metal oxides, metal hydroxides and metal hydroxide salts in aqueous solution, Pure Appl. Chem. 6 (1963) 125–206.